AGU ADVANCING EARTH AND SPACE SCIENCE

Geophysical Research Letters®

RESEARCH LETTER
10.1029/2022GL099758

Micromagnetic Modes of Anisotropy of Magnetic Susceptibility in Natural Magnetite Particles

Even S. Nikolaisen[1], Karl Fabian[1], Richard Harrison[1,2], and Suzanne A. McEnroe[1]

[1]Norwegian University of Science and Technology (NTNU), Trondheim, Norway, [2]Department of Earth Sciences, University of Cambridge, Cambridge, UK

Key Points:

- Micromagnetics and nanotomography elucidate the physical anisotropy of magnetic susceptibility (AMS) modes of natural magnetite particles
- The data explain the transition from inverse to normal AMS fabric with increasing grain size
- A systematic characterization of AMS modes in single-domain and pseudo-single domain magnetite particles is established

Supporting Information:

Supporting Information may be found in the online version of this article.

Correspondence to:

E. S. Nikolaisen,
even.nikolaisen@ntnu.no

Citation:

Nikolaisen, E. S., Fabian, K., Harrison, R., & McEnroe, S. A. (2022). Micromagnetic modes of anisotropy of magnetic susceptibility in natural magnetite particles. *Geophysical Research Letters*, *49*, e2022GL099758. https://doi.org/10.1029/2022GL099758

Received 2 JUN 2022
Accepted 15 AUG 2022

Author Contributions:

Conceptualization: Even S. Nikolaisen, Karl Fabian
Data curation: Even S. Nikolaisen
Formal analysis: Richard Harrison
Funding acquisition: Richard Harrison, Suzanne A. McEnroe
Methodology: Even S. Nikolaisen, Karl Fabian
Project Administration: Richard Harrison, Suzanne A. McEnroe
Software: Karl Fabian
Supervision: Karl Fabian, Richard Harrison, Suzanne A. McEnroe
Validation: Karl Fabian, Richard Harrison, Suzanne A. McEnroe
Visualization: Even S. Nikolaisen

Abstract

Anisotropy of magnetic susceptibility (AMS) is commonly used to assess sedimentation, deformation, tectonics, rock fabric, and texture. Using focused-ion beam nanotomography, we develop a micromagnetic method to investigate the AMS of individual magnetite inclusions in silicates across the transition between single-domain (SD) to multidomain behavior. We calculate individual AMS tensors by modeling the magnetization response of a particle to weak applied fields in three orthogonal directions. The main AMS mode of elongated SD particles is not a homogeneous magnetization rotation, but focused alignment of spins at their edges and tips. In single-vortex particles, vortex displacement is the dominant AMS mode, which focuses the largest magnetization changes in a planar region containing the vortex core, and perpendicular to the direction of vortex motion. In multi-vortex structures a combined motion of all vortex centers can lead to high degrees of anisotropy when some motion patterns are energetically much easier to achieve than others.

Plain Language Summary

Many rocks have physical properties that vary according to the direction in which these are measured. Such rocks are called anisotropic. A fast and simple measurement which can uncover such anisotropy is the magnetization response to applied fields in different directions. This anisotropy of magnetic susceptibility (AMS), or AMS, is used in numerous applications to detect hidden information about geological processes. However, the interpretation of AMS data requires additional knowledge about the small magnetic mineral grains in the rock, because very small grains behave exactly opposite (inverse) to very large grains (normal). Here, we use hundreds of slices of electron microscopy images to reconstruct the exact shape of hundreds of such tiny magnetite grains. Then we run computer models to predict how these grains respond to applied magnetic fields. These data reveal how magnetic grains react to magnetic fields, and help us to understand better why small and large grains behave differently. Now we have a much better insight into the physical processes that are measured during AMS determinations made in laboratories all over the world.

1. Introduction

Anisotropy of magnetic susceptibility (AMS) is a trusted magnetic technique in studies of petrofabric and structural geology (Biedermann & Bilardello, 2021; Borradaile, 1988; Hrouda, 1982; Jackson & Tauxe, 1991; Lowrie, 1989; Owens & Bamford, 1976). In individual ferrimagnetic particles the magnetic susceptibility (MS) originates from a change of the magnetization structure in response to a small applied field. Shape anisotropy of individual ferrimagnetic particles creates AMS if they have a shape preferred orientation (SPO). In normal SPO fabrics, the direction of maximal MS is aligned with the preferred particle elongation axis, and the direction of minimal MS with the shortest axis. Axis ratio and SPO depend on sedimentation, liquid flow, deformation, crystal growth and orientation of exsolved magnetic grains. Only distribution anisotropy (Hargraves et al., 1991) requires no individual particle anisotropy as it originates from an anisotropic interaction field.

AMS at different field strengths and temperatures provides AMS ellipsoids as sketched in Figure 1a with principal axes $\mathbf{V}_1$, $\mathbf{V}_2$, $\mathbf{V}_3$ and susceptibilities $\chi_1 \geq \chi_2 \geq \chi_3$ (Biedermann, 2018; Bilardello, 2016; Nye, 1985; Rochette et al., 1992). For interpretation, up to 30 derived parameters are available (Tarling & Hrouda, 1993), of which the most common are the mean susceptibility $K_m = (\chi_1 + \chi_2 + \chi_3)/3$ and the three anisotropy ratios $L = \chi_1/\chi_2$ (lineation), $F = \chi_2/\chi_3$ (foliation) and $P = \chi_1/\chi_3$ (degree of anisotropy) (Ellwood et al., 1988; Rochette et al., 1992).

Current AMS theory is based on two extreme cases. Single-domain (SD) theory assumes homogeneous magnetization in the magnetite particles, rotating toward an applied magnetic field. Inverse, or intermediate magnetic fabric in some magnetite bearing rocks can originate from the inverse relation between geometric and magnetic

Writing – original draft: Even S. Nikolaisen
Writing – review & editing: Even S. Nikolaisen, Karl Fabian, Richard Harrison, Suzanne A. McEnroe

axes in SD magnetite particles because they easily rotate perpendicular to their elongated easy axis, and have zero MS along this axis (Potter & Stephenson, 1988; Rochette et al., 1992). For multidomain (MD) magnetite MS is assumed to be controlled exclusively by the demagnetizing tensor which directly reflects particle shape and predicts highest MS along the longest axis, and least MS along the shortest axis (Rochette et al., 1992; Stephenson et al., 1986). This was confirmed for polycrystalline magnetite by Uyeda et al. (1963). The AMS behavior of pseudo-single domain (PSD) particles has been an open problem since the late 1980s where bulk measurements indicated that inverse fabrics may also be related to PSD sizes (Rochette et al., 1992).

To date, the exact modes of AMS in small particles have not been quantitatively studied. By combining focused ion beam nanotomography and micromagnetic modeling we investigate from first principles the AMS of individual natural magnetite particles hosted in pyroxene and plagioclase. Our particle collection was previously described in Nikolaisen, Harrison, et al. (2022), where anisotropy of remanent magnetization and AMS from saturated hysteresis was studied. Here we extend these results by modeling conventional AMS measurements and calculate the MS of the lowest determined energy minima for >300 naturally formed magnetite particles. We test and modify the current theoretical concepts how shape, size, domain state and internal mechanisms affect the AMS of individual magnetite particles.

2. Methods

2.1. Focused Ion Beam Nanotomography

We use particle shapes from two focused ion beam (FIB) locations on a thin section (B-16) from the Roossenekal Main Zone profile of the Bushveld eastern lobe 145 m below the pyroxenite marker (Cawthorn et al., 2016; Lundgaard et al., 2006). Experimental details are described in Nikolaisen, Harrison, et al. (2022). Particle meshes from the orthopyroxene ($Mg_{60.2\pm0.2}$) and plagioclase ($An_{62.6\pm0.9}$) FIB locations (Nikolaisen, Harrison, et al., 2022), and stereolithography files are available at https://doi.org/10.18710/AZT6UY [doi]. From the MERRILL meshes we calculate a geometric shape tensor based on the symmetric inertia tensor normalized by mass and volume. The shape ellipsoid is defined by its inverse eigenvalues $L_1 \geq L_2 \geq L_3$ and principal axes $\mathbf{L}_1$, $\mathbf{L}_2$, $\mathbf{L}_3$.

2.2. Calculation of Magnetic Susceptibility

Our AMS calculations use MERRILL 1.3.5 (Conbhuí et al., 2018; Fabian & Shcherbakov, 2018) with magnetite material parameters at 20°C. The cubic anisotropy axes were oriented along the FIB coordinate axes, because we do not have sufficient control over the detailed orientation of the host minerals (Ageeva et al., 2020, 2022; Bown & Gay, 1959; Nikolaisen, Harrison, et al., 2022) and cubic magnetocrystalline anisotropy does not contribute to individual particle AMS. We start by minimizing 25 or 50 different random initial states and choosing the lowest local energy minimum (LLEM) as approximation to the absolute energy minimum. We used 50 minimizations only if the first 25 required less than 24 hr.

For each particle the AMS tensor $\mathbf{X}$ was initially approximated from six minimization runs of the LLEM along fields in the FIB $\pm x$, $\pm y$, $\pm z$-directions. In each run field strength h was from 0 to 5 mT by 1 mT increments.

For each point $\mathbf{p}$ on the unit sphere S^2 one could measure the MS $\chi(\mathbf{p}) = \chi(-\mathbf{p})$, such that the real valued function

$$\chi : S^2 \to \mathbb{R}, \quad \mathbf{p} \mapsto \chi(\mathbf{p}),$$

assigns to each measurement direction the corresponding MS and thus defines a point symmetric AMS surface. Our initial MERRILL calculations in directions $\mathbf{e}_i$ with $i = x, y, z$ for different field strengths h provide magnetization vectors $\mathbf{m}_j(h\,\mathbf{e}_i)$ from which the ij-coefficients of the AMS tensor

$$\chi_{ij} = \frac{m_j(h\,\mathbf{e}_i) - m_j(0)}{h}, \quad i, j = x, y, z,$$

are calculated by fitting straight lines through the minimizations between $h = -5$ and $h = 5$ mT. The χ_{ij} define a tensor of MS which is symmetrized by

$$\chi_{ij}^{\mathrm{sym}} = \frac{\chi_{ij} + \chi_{ji}}{2}.$$

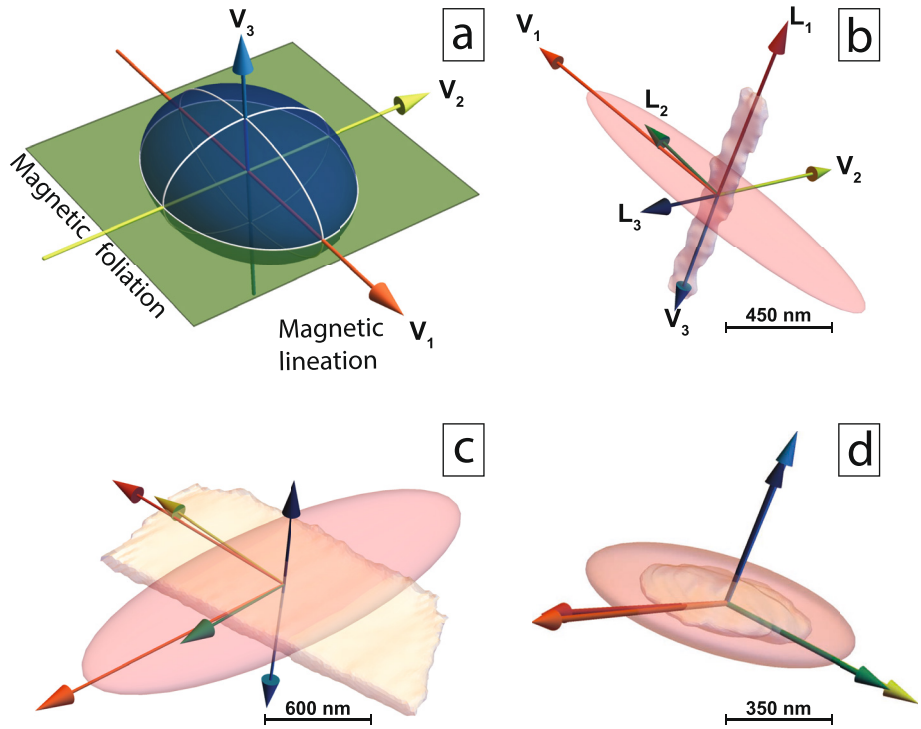

Figure 1. (a) Schematic anisotropy of magnetic susceptibility (AMS) ellipsoid with principal axes $\mathbf{V}_1$, $\mathbf{V}_2$, $\mathbf{V}_3$ and eigenvalues $\chi_1 \geq \chi_2 \geq \chi_3$ which define the magnetic foliation F and magnetic lineation L. (b) Principal axes of particle shape (dark red, dark green, and dark blue) in comparison to the AMS ellipsoid (light red) with principal axes $\mathbf{V}_1$, $\mathbf{V}_2$, $\mathbf{V}_3$ (orange, light green, and light blue) for prolate single-domain particle OPX070 with inverse fabric. (c) Principal axes of the shape and AMS for an oblate multi-vortex particle OPX040 with intermediate fabric (same color scheme). (d) Principal axes of the shape and AMS for an oblate single-vortex particle OPX001 with normal fabric (same color scheme).

By diagonalizing χ_{ij}^{sym}, we determine principal axes $\mathbf{V}_1$, $\mathbf{V}_2$, $\mathbf{V}_3$ and corresponding eigenvalues $\chi_1 \geq \chi_2 \geq \chi_3$, which approximate the AMS tensor $\mathbf{X}$ if the true AMS surface does not deviate too much from an ellipsoid.

2.3. AMS Eigenmodes and Their Visualization

In the second MERRILL calculation, we apply the fields directly along the previously obtained principal axes $\mathbf{V}_1$, $\mathbf{V}_2$, $\mathbf{V}_3$. This leads to new susceptibilities

$$\chi'_{ij} = \frac{m_j(h\,\mathbf{V}_i) - m_j(0)}{h}, \quad i,j = 1,2,3,$$

which define a second approximation $\mathbf{X}'$ to the AMS tensor. Ideally, $\mathbf{X}'$ is diagonal and equivalent to $\mathbf{X}$ with diagonals $\chi'_i \approx \chi_i$ for $i = 1, 2, 3$ and $\chi'_{ij} \approx 0$ for $i \neq j$. This request can be transformed into a quality parameter

$$Q = \frac{\sqrt{{\chi'_{11}}^2 + {\chi'_{22}}^2 + {\chi'_{33}}^2}}{\|\mathbf{X}'\|},$$

which is close to 1 if $\mathbf{X}'$ is nearly diagonal along $\mathbf{V}_1$, $\mathbf{V}_2$, $\mathbf{V}_3$. If this applies, one can drop the distinction between $\mathbf{X}$ and $\mathbf{X}'$. The magnetization changes along the principal axes define three AMS eigenmodes, which can be visualized in different ways. Direct inspection as in Figure 2, can delineate the positions of the vortex cores by their corresponding helicity isosurfaces (green for $h = -5$ mT, yellow $h = +5$ mT). The first two AMS eigenmodes are movements of the vortex core almost perpendicular to the applied field resembling domain wall motions. The third eigenmode along the view axis involves an overall tilt of all moments out of the plane. Only this mode was previously analyzed in a simplified model of cylindrical vortex particles (Heider et al., 1996).

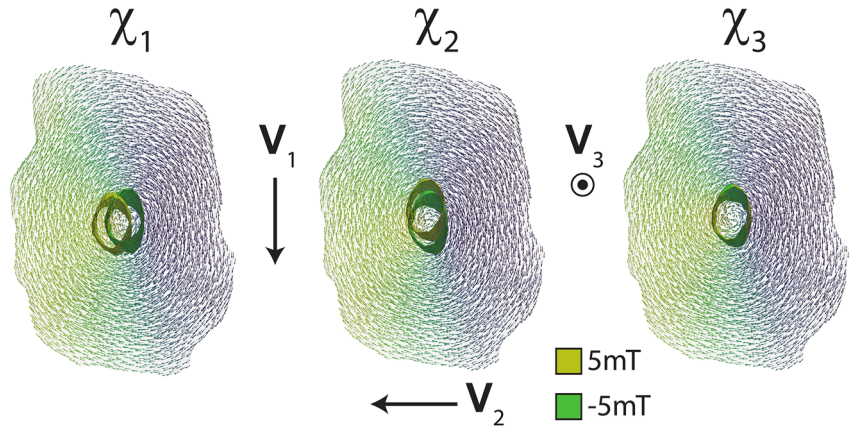

Figure 2. Vortex center of the single-vortex lowest local energy minimum for OPX001. Isosurfaces of helicity represent the movement of the vortex center in field strength from −5 mT (green) to 5 mT (yellow). Left: Eigenmode $\mathbf{V}_1$ for $\chi_1 = 9.4$ SI with field pointing approximately downward, such that the domain of blue spins increases with increasing field, and the vortex core moves to the left. Center: Corresponding vortex motion in the eigenmode $\mathbf{V}_2$ approximately pointing to the left and $\chi_2 = 6.3$ SI. Right: Almost no vortex motion for eigenmode $\mathbf{V}_3$ approximately pointing into the plane and $\chi_3 = 1.5$ SI.

The eigenmodes related to the $\mathbf{V}_i$ can also be compared by visualizing at each mesh node the difference vector $\Delta\mathbf{m}$ between $\mathbf{m}(h\,\mathbf{V}_i)$ and $\mathbf{m}(-h\,\mathbf{V}_i)$ for $h = 5$ mT, to indicate where the significant magnetization changes occur (Figure 3). Eigenmode visualizations for all modeled particles are provided in the associated modeling report (M-report) (DataverseNO: Nikolaisen, Fabian, et al., 2022).

3. Results

3.1. AMS Mechanisms in Different Magnetic Domain Structures

Figure 3 represent initial LLEM states for three of the >300 modeled particles. The three right panels in each row display $\Delta\mathbf{m}$ for the eigenmodes along $\mathbf{V}_1$, $\mathbf{V}_2$, $\mathbf{V}_3$, and the stereoplot displays the directions of $\mathbf{V}_1$, $\mathbf{V}_2$, $\mathbf{V}_3$ in relation to the geometric principal axes with lengths $L_1 \geq L_2 \geq L_3$.

Homogeneous rotation is observed only for very small and nearly equidimensional SD particles like PLAG238, whilst for most SD grains, the dominant AMS modes primarily change the magnetization near the tips and little in the center. The top row of Figure 3 shows a typical localized χ_1 mode for a long SD particle where the tip magnetizations rotate more strongly in the $\mathbf{L}_2$ direction than the central parts. Here the χ_2 mode with out-of-plane magnetization change corresponds better to the classical homogeneous rotation. Because the remanent magnetization is oriented parallel to $\mathbf{L}_1$, the lowest χ_3 mode points along this direction and the magnetization changes are again localized at the tips where the outward bending spins of the flower state can be aligned with the field. Another localized χ_1 mode occurs in SD particles with a buckling-type (undulating) magnetization structure, for example, OPX009 in the M-report.

To quantify the localization of AMS modes, the M-report contains for each mode $\mathbf{V}_j$, $j = 1, 2, 3$ the statistical distribution of the normalized mesh-node susceptibilities

$$d(k) \;:=\; \frac{\mu_0\, M_s\, \mathrm{vol(k)}\; (\Delta\mathbf{m}\cdot\mathbf{V}_j)\,/\Delta B - \chi_j\, \mathrm{vol(k)}}{\chi_j\, \mathrm{vol}},$$

where vol(k) is the volume represented by node k, vol is the total particle volume, and the field difference is $\Delta B = 10$ mT. The histogram of a mode has a narrow peak around zero, if all nodes contribute equally to χ_j, corresponding to a global susceptibility mode. Localized modes show very broad or bimodal distributions.

The dominant magnetization change of single-vortex (SV) and multi-vortex (MV) structures occurs in the interior of the particle by vortex movement as displayed in Figure 2. These dominant modes enlarge the volume of magnetizations that are aligned with the applied field, and diminish the volume that is oppositely magnetized. In this respect they correspond to domain wall motion. Modes where the magnetization of the vortex center is

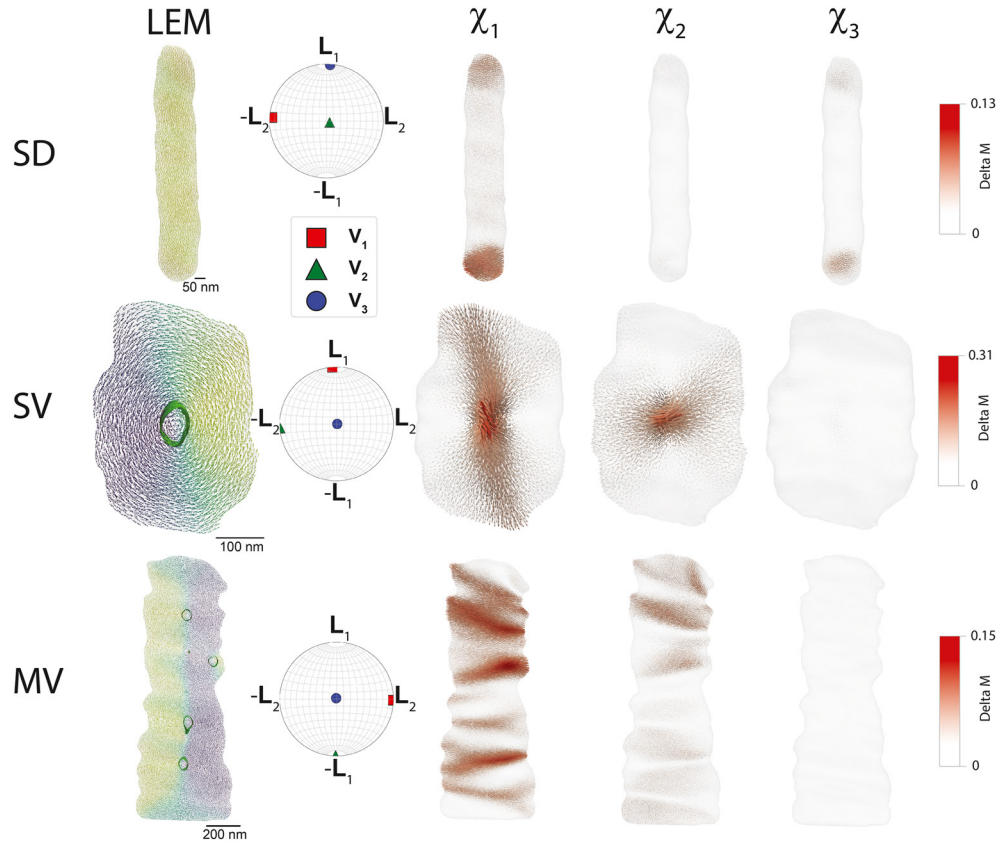

Figure 3. Anisotropy of magnetic susceptibility (AMS) eigenmodes for three particles with different sizes and domain structures. All particles are oriented in the same directions within the host crystal. For each particle the structure of the LEM state with lowest energy found is shown on the left side. The remaining three plots reflect the difference vectors **Δm** for field changes along the eigendirections of the AMS tensor. **Δm** is calculated from the magnetization structures in fields of 5 and −5 mT along these directions. The corresponding eigenvalues or susceptibilities are 4.7, 1.7, 0.6 for the single-domain (SD) state, 9.4, 6.3, 1.5 for the single-vortex state, and 15.2, 2.3, 1.2 for the multi-vortex state. The color scale for the lowest local energy minimum plot reflects the magnetization direction for each node (yellow: up, purple: down). The color scale for the eigenvectors represents the lengths |**Δm**| scaled by the largest difference in the respective particle.

rotated toward the applied field, or global modes where all vortex spins improve their alignment with a field along the vortex axis are related to smaller susceptibilities, mostly χ_3 as in the SV, MV cases of Figure 3.

In SV particles $\mathbf{V}_1$ is usually aligned with the elongation direction as in Figure 3, because the elliptically stretched vortex forms the precursor of a single Bloch wall separating two main domains magnetized in opposite directions along the elongation axis. MV particles with multiple vortices are precursors of MD structures. If they are elongated, their modes of magnetization change differ from the simple vortex motion of SV particle (Figure 3). Their vortex centers move more easily along the medium geometrical axis $\mathbf{L}_2$ with very little change along $\mathbf{L}_1$.

3.2. AMS of Single Particles

The mean MS over all particles and directions is $\bar{\chi} = 4.93$ SI. The degree of anisotropy $P = \chi_1/\chi_3$ clearly decreases with increasing size for SD particles <0.1 μm, but then scatters within an interval of 2–100 independent of particle size or magnetic domain state (Figure 4a).

The Flinn plot in Figure 4b represents the shape of the AMS ellipsoids for the individual particles. SD particles in our samples mainly occur in spherical to prolate shapes (Figure 4c) which are related to oblate AMS ellipsoids (Figure 4b), where usually χ_3 is much smaller than χ_2 as illustrated in the sketches in Figures 1b–1d. Comparing the geometric lineation of SD particles against P in Figure S1 of Supporting Information S1, show two trends that are divided by particle size. For particles >0.1 μm, P shows a parabolic increase with an increase of geometric

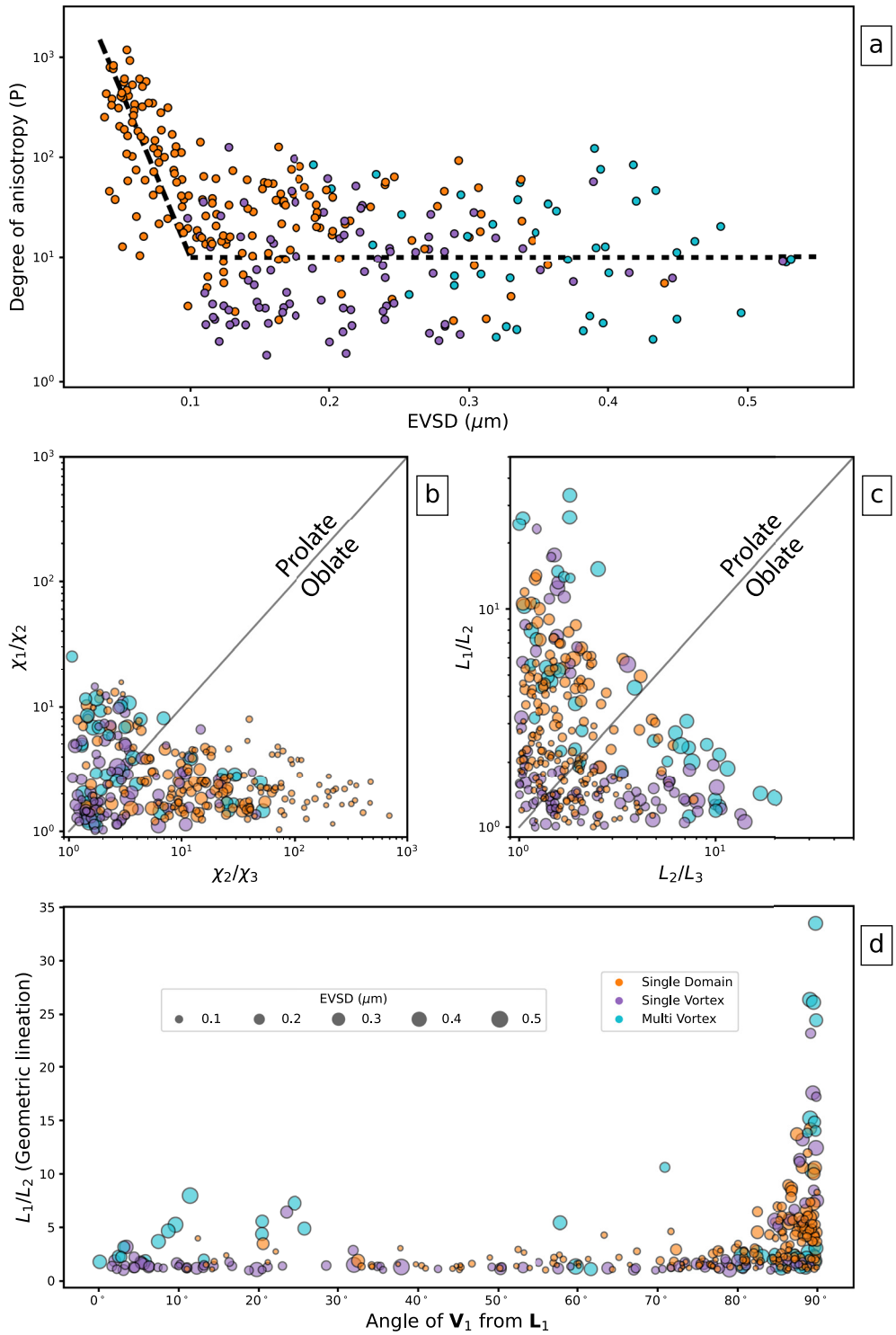

Figure 4. Flinn diagrams for natural magnetite particles orthopyroxene, plagioclase. (a) Flinn diagram for shape parameters of anisotropy of magnetic susceptibility (AMS) eigenvalues $\chi_1 > \chi_2 > \chi_3$. Colors indicate lowest local energy minimum magnetization structure, symbol size encodes particle equivalent volume sphere diameter (EVSD). (b) Corresponding Flinn diagram for shape eigenvalues $L_1 > L_2 > L_3$. (c) Relation between EVSD and anisotropy degree $P = \chi_1/\chi_3$. (d) L_1/L_2 geometric lineation) versus acute angle $\angle \mathbf{V}_1\mathbf{L}_1$. This angle is 0° for normal AMS fabric and 90° for inverse fabric. The legend applies to all sub-figures.

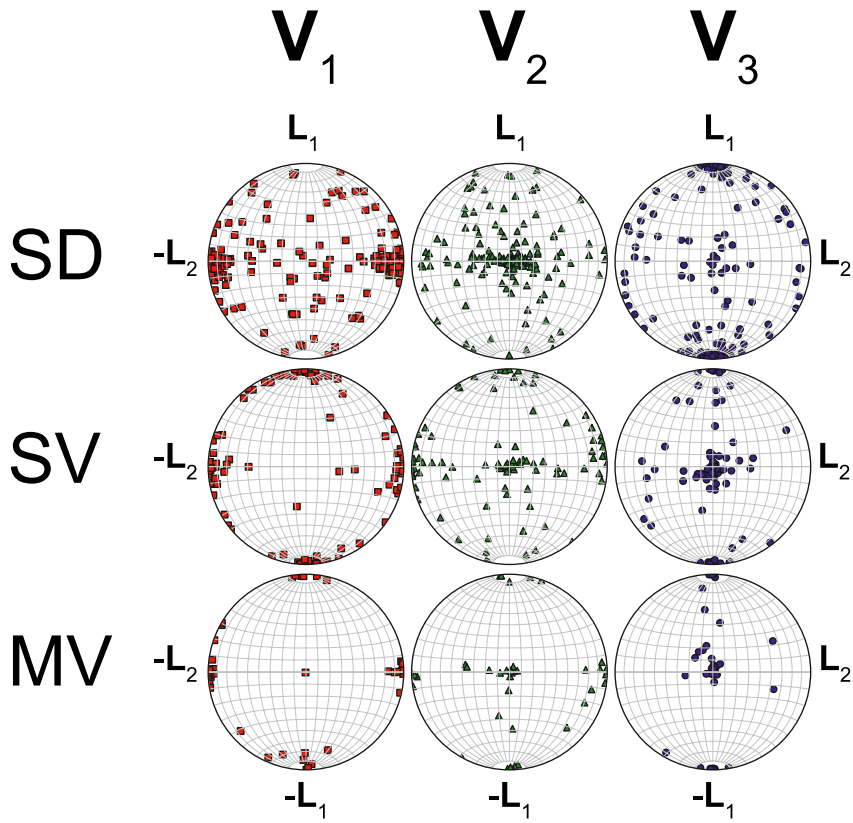

Figure 5. Anisotropy of magnetic susceptibility (AMS) eigendirections for single-domain (SD), single-vortex (SV), multi-vortex (MV) states. The stereonets project AMS eigendirections along $\mathbf{L}_3$ with $\mathbf{L}_1$ up and$\mathbf{L}_2$ right. SD particles (top row) display an inverse magnetic fabric, where $\mathbf{V}_1\|\mathbf{L}_2$ and $\mathbf{V}_3\|\mathbf{L}_1$. For SV and MV states the magnetic fabric transits to normal orientation with apparent $\mathbf{V}_3\|\mathbf{L}_3$ and increasing population of $\mathbf{V}_1\|\mathbf{L}_1$.

lineation and particle size (dotted line). The smaller particles <0.1 μm (yellow background) do not follow this trend, but in general reflect elevated *P* without connection to the geometric lineation. When comparing geometric foliation against *P*, the same particle size range (<0.1 μm) as in Figure S2 of Supporting Information S1 for SD particles are also here highlighted in yellow background. Prolate particles in this size range do show a decreasing *P* with an increasing geometric foliation, where oblate particles show the opposite trend.

SV particles (Figure S1 in Supporting Information S1) reflect trends (dotted lines) where *P* increases with an increasing geometric lineation. As for particle size, there is a trend of an increasing *P* with an increasing particle size. For MV particles, an increase in geometric lineation result in a decrease of *P*. This trend is linear for prolate and oblate particles until the length to width ratio >10 (red tinted background) where *P* increases significantly. For these specific prolate particles, *P* continues to increase with increasing geometric lineation. With an increase of geometric foliation (Figure S2 in Supporting Information S1) the larger SD, SV, and MV particles indicate general trends (dotted lines) of increasing *P*. These trends of increasing *P* with geometric foliation in SV and MV are dominated by oblate particles, which become more distinct for MV domain states.

In Figure 5 SD particles show an inverse magnetic fabric in relation to the particle axes, where $\mathbf{V}_1\|\mathbf{L}_2$, $\mathbf{V}_2\|\mathbf{L}_3$, and $\mathbf{V}_3\|\mathbf{L}_1$. There are SD particles that deviate from the inverse relation with $\mathbf{V}_1$ trending toward $\mathbf{L}_3$. These points are explained by two separated occurrences that are overlapping. Particles where $\mathbf{V}_1$ drifts toward $\mathbf{L}_3$ are represented by long SD needles in the plagioclase. Other points that plot away from the directions of $\mathbf{L}_2$ and $\mathbf{L}_3$ are for small (equivalent volume sphere diameter [EVSD] <0.1 μm) oblate particles. For particles with SV and MV domain states there starts to form a cluster of $\mathbf{V}_1\|\mathbf{L}_1$ and increasing population densities of $\mathbf{V}_2\|\mathbf{L}_2$ and $\mathbf{V}_3\|\mathbf{L}_3$.

4. Discussion

4.1. MS and AMS of Single Magnetite Particles

The average mean MS for our >300 particles is 4.9 SI, well above the calculations and data of Heider et al. (1996) for synthetic and natural magnetite with 3.1 ± 0.4 SI, probably because their calculations use rather low MS modes. In contrast to our modeled non-interacting particles, the lower measurements from the real magnetite samples of Heider et al. (1996) mainly come from strongly interacting isotropic samples, for which the sample MS χ is related to particle MS χ_p by

$$\chi = \chi_p / (1 + N\,\chi_p) < \chi_p,$$

where $N > 0$ is the average isotropic demagnetizing factor of the sample (Stacey & Banerjee, 1974).

In the size range (<0.1 μm), the degree of anisotropy decreases exponentially (Figure 4c). This is generated by spherical to oblate SD particles with a very low and even negative χ_3. For particles >0.1 μm P is confined to $100 > P > 0$ with no apparent dependency on equivalent volume sphere diameter (EVSD). This is expected, because cubic minerals are magnetically isotropic and AMS thus primarily depends on shape not volume (Stoner, 1945; Uyeda et al., 1963).

The M-report provides a comprehensive overview over a large variety of single particle domain states and AMS tensors for natural magnetite grains in the Single-domain-pseudo-single domain transition region. Due to the high variability in size and shape, these tensors do not behave in a regular and easily explainable fashion. Yet, Figure 4 together with the associated Figures S1 and S2 in Supporting Information S1 indicate certain trends.

The most pronounced trend in Figure 4c is the mentioned decrease of P with increasing EVSD below an EVSD of 0.1 μm. Other less prominent trends are domain-state dependent changes in the degree of geometric lineation in Figure S1 of Supporting Information S1, where geometrically prolate SD and SV states show a weak parabolic increase of P with increasing geometric lineation for particles with EVSD >0.1 μm. MV states with geometric lineation <10 decrease in P as a function of L_1/L_2. At $L_1/L_2 = 10$ there is an abrupt increase in P and the trend continues with positive slope. This may indicate a general transition in the vortex arrangement for these needle-or whisker-like particle shapes, where a formation of closure domains or vortices at the tips allows for high-susceptibility modes along $\mathbf{L}_1$.

Figure S2 in Supporting Information S1 plots the degree of anisotropy $P = \chi_1/\chi_3$ versus geometric foliation (L_2/L_3). The different domain states, SD, SV and MV show a similar increase of minimal P with increasing L_2/L_3 (dotted lines). For SV and MV states, this trend is defined mainly by oblate particles, and also seems to be related to increased ease of vortex motion with increased particle width.

4.2. Transition From Inverse to Normal Fabric

SD particles with inverse magnetic fabric are generally prolate with EVSD >0.1 μm. This agrees with bulk measurements (Potter & Stephenson, 1988; Stephenson & Potter, 1987; Stephenson et al., 1986), where for SD particles $\mathbf{V}_1$ aligns with $\mathbf{L}_2$ and $\mathbf{V}_3$ with $\mathbf{L}_1$. Our data set contains also SD particles with EVSD <0.1 μm and L_1/L_2 approaching 1, where $\mathbf{V}_1$ deviates from the $\mathbf{L}_2$ axis, and is not oriented in any recognizable relation to the shape tensor. The calculated results often reflect $\chi_1 > \chi_2 \gg \chi_3$, where χ_3 can even be negative.

Above the SD/SV transition, a normal magnetic fabric starts to develop (Figure 5), whereby the $\mathbf{v}_3$ axis for SV and MV particles aligns best to its normal position, which is along L_3, whilst the alignment of v_1 with L_1 is less clearly visible. Several of the SV/MV particles also carry a rotated normal fabric. This we observe particularly in elongated particles of varying particle size. Figure 3 visually presents one such MV particle (OPX019), where the LEM shows multiple vortex cores aligned in direction of $\mathbf{L}_1$. Our hypothesis is that one or more vortices close to the edge of the particle can undergo significant changes with even the slightest adjustments of the external field strength. Resulting in small areas of the particle that contribute to high susceptibility in certain directions. This can be an effect of our minimizations from a random state that are unable to locate the absolute lowest energy minimum, therefore creating magnetic structures that are easily susceptible to change. However, the same effects are observed for SV particles with varying length to width ratio (Figure 4d). Our detailed observations of magnetic fabric expand on bulk AMS studies by (Potter & Stephenson, 1988; Stephenson & Potter, 1987;

Stephenson et al., 1986) of the AMS ellipsoid for magnetite, who determined that in a prolate MD particles the direction of $\mathbf{V}_1$ is parallel to $\mathbf{L}_1$.

Because the particles within this study do not contain large MD structures, it is possible that there exists a transition beyond the MV state that favors a normal magnetic fabric. Within the size range of our study the normal magnetic fabrics are only observed for particles where $L_1/L_2 < 10$ (Figure 4d and Figure S3 in Supporting Information S1). Prolate MV particles, for example, magnetite needles in the plagioclase, express a rotated normal magnetic fabric. Here, $\mathbf{V}_1$ is oriented parallel to $\mathbf{L}_2$, but differs from an inverse magnetic fabric with $\mathbf{V}_3 \| \mathbf{L}_3$.

In Figure 4d and Figure S3 of Supporting Information S1, this effect is also visible, and indicates that for individual PSD magnetite particles the magnetic foliation is the best determined normal anisotropy, whilst magnetic lineation represents the L_3 with smaller accuracy. It may therefore be beneficial to rather use the average normal to a collection of v_3 directions to determine flow directions from PSD magnetite carriers.

4.3. Thermally Activated Transitions Across Energy Barriers

Here we only analyze changes in thermally stable magnetization structures, and do not include thermally activated energy barriers, which is a topic of further investigation. In several LLEM structures, applying a small field <5 mT leads to irreversible magnetization changes, indicated by relatively low $Q < 0.99$. This typically occurs in large and extremely oblate particles (e.g., OPX029, OPX050, and OPX051) and requires separate investigation of energy barriers and thermal stability (Fabian & Shcherbakov, 2018). We also do not include thermally activated superparamagnetic SD particles, because they are perfectly homogeneous and very well described by Néel theory. Maher (1988) and Lanci and Zanella (2016) provide experimental and theoretical studies of the corresponding increase in MS and its influence on AMS.

5. Conclusion

Based on magnetite particle meshes from FIB nanotomography we develop a micromagnetic method to calculate approximate AMS tensors for more than 300 particle shapes. We identify, characterize, and visualize the principal AMS magnetization modes for natural SD and PSD grains. We find that high MS modes, even for SD particles, are usually due to local magnetization changes related to flowering, buckling, or vortex motion. Global modes of SD tilting, or vortex stretching mostly lead to lower MS. The found AMS modes are related to the transition between inverse and normal fabrics in magnetite-bearing samples, whereby SD particles in general reflect an inverse magnetic fabric, with spherical to highly oblate AMS ellipsoids. With increasing domain state complexity a gradual transition to a normal magnetic fabric occurs, whereby χ_3 aligns easier with $\mathbf{L}_3$ than χ_1 with $\mathbf{L}_1$, such that PSD magnetite may be more reliable for magnetic foliation than for magnetic lineation. This study opens a new path toward a detailed physical understanding of AMS in geological contexts. Further, this work provides new insight into inverse PSD fabrics and underlines the importance of fully understanding the magnetic mineral assemblages in AMS studies.

Data Availability Statement

All data for recreating the results, presented in this study are available at DataverseNO (https://doi.org/10.18710/B7BWXO).

Acknowledgments
The FIB-SEM and Slice-and-View work was performed at the NTNU Nanolab and the Norwegian infrastructure for micro- and nanofabrication as part of a PhD-project funded by NTNU. The Research Council of Norway is acknowledged for the support to the Norwegian Micro-and Nano-Fabrication Facility, NorFab, Project 245963/F50. The calculations and usage of a Linux server was possible with granted access by IGP and a designated workstation with remote access. The authors thank Olivia Moehl for substantial help with data processing and visualization.

References

Ageeva, O., Bian, G., Habler, G., Pertsev, A., & Abart, R. (2020). Crystallographic and shape orientations of magnetite micro-inclusions in plagioclase. *Contributions to Mineralogy and Petrology*, *175*(10), 1–16. https://doi.org/10.1007/s00410-020-01735-8

Ageeva, O., Habler, G., Gilder, S. A., Schuster, R., Pertsev, A., Pilipenko, O., et al. (2022). Oriented magnetite inclusions in plagioclase: Implications for the anisotropy of magnetic remanence. *Geochemistry, Geophysics, Geosystems*, *23*(2), e2021GC010272. https://doi.org/10.1029/2021gc010272

Biedermann, A. R. (2018). Magnetic anisotropy in single crystals: A review. *Geosciences*, *8*(8), 302. https://doi.org/10.3390/geosciences8080302

Biedermann, A. R., & Bilardello, D. (2021). Practical magnetism vii: Avoiding common misconceptions in magnetic fabric interpretation. *The IRM Quarterly*.

Bilardello, D. (2016). Magnetic anisotropy: Theory, instrumentation, and techniques. *Reference Modules in Earth Systems and Environmental Sciences*.

Borradaile, G. J. (1988). Magnetic susceptibility, petro fabrics and strain. *Tectonophysics*, *156*(1–2), 1–20. https://doi.org/10.1016/0040-1951(88)90279-x

Bown, M., & Gay, P. (1959). The identification of oriented inclusions in pyroxene crystals. *American Mineralogist: Journal of Earth and Planetary Materials*, *44*(5–6), 592–602.

Cawthorn, R. G., Lundgaard, K. L., Tegner, C., & Wilson, J. R. (2016). Lateral variations in plagioclase compositions, main zone, bushveld complex, south Africa: Evidence for slow mixing of magmas in basinal structures. *Mineralogical Magazine*, *80*(2), 213–225. https://doi.org/10.1180/minmag.2015.079.7.12

Conbhuí, P. Ó., Williams, W., Fabian, K., Ridley, P., Nagy, L., & Muxworthy, A. R. (2018). MERRILL: Micromagnetic Earth related robust interpreted language laboratory. *Geochemistry, Geophysics, Geosystems*, *19*(4), 1080–1106. https://doi.org/10.1002/2017gc007279

Ellwood, B. B., Hrouda, F., & Wagner, J.-J. (1988). Symposia on magnetic fabrics: Introductory comments. *Physics of the Earth and Planetary Interiors*, *51*(4), 249–252. https://doi.org/10.1016/0031-9201(88)90066-0

Fabian, K., & Shcherbakov, V. P. (2018). Energy barriers in three-dimensional micromagnetic models and the physics of thermoviscous magnetization. *Geophysical Journal International*, *215*(1), 314–324. https://doi.org/10.1093/gji/ggy285

Hargraves, R. B., Johnson, D., & Chan, C. Y. (1991). Distribution anisotropy: The cause of AMS in igneous rocks? *Geophysical Research Letters*, *18*(12), 2193–2196. https://doi.org/10.1029/91gl01777

Heider, F., Zitzelsberger, A., & Fabian, K. (1996). Magnetic susceptibility and remanent coercive force in grown magnetite crystals from 0.1 μm to 6 mm. *Physics of the Earth and Planetary Interiors*, *93*(3–4), 239–256. https://doi.org/10.1016/0031-9201(95)03071-9

Hrouda, F. (1982). Magnetic anisotropy of rocks and its application in geology and geophysics. *Geophysical Surveys*, *5*(1), 37–82. https://doi.org/10.1007/bf01450244

Jackson, M., & Tauxe, L. (1991). Anisotropy of magnetic susceptibility and remanence: Developments in the characterization of tectonic, sedimentary, and igneous fabric. *Reviews of Geophysics*, *29*(S1), 371–376. https://doi.org/10.1002/rog.1991.29.s1.371

Lanci, L., & Zanella, E. (2016). The anisotropy of magnetic susceptibility of uniaxial superparamagnetic particles: Consequences for its interpretation in magnetite and maghemite bearing rocks. *Journal of Geophysical Research: Solid Earth*, *121*, 27–37. https://doi.org/10.1002/2015jb012255

Lowrie, W. (1989). Magnetic analysis of rock fabric. *James, DE The Encyclopedia of Solid Earth Geophysics*, 698–706.

Lundgaard, K. L., Tegner, C., Cawthorn, R. G., Kruger, F. J., & Wilson, J. R. (2006). Trapped intercumulus liquid in the main zone of the eastern bushveld complex, South Africa. *Contributions to Mineralogy and Petrology*, *151*(3), 352–369. https://doi.org/10.1007/s00410-006-0063-x

Maher, B. A. (1988). Magnetic properties of some synthetic sub-micron magnetites. *Geophysical Journal International*, *94*(1), 83–96. https://doi.org/10.1111/j.1365-246x.1988.tb03429.x

Nikolaisen, E. S., Fabian, K., Harrison, R. J., McEnroe, S. A., & Moehl, O. (2022). *Replication data for: Micromagnetic modes of the anisotropy of magnetic susceptibility in natural magnetite particles* [dataset]. DataverseNO. https://doi.org/10.18710/B7BWXO

Nikolaisen, E. S., Harrison, R., Fabian, K., Church, N., McEnroe, S. A., Sørensen, B. E., & Tegner, C. (2022). Hysteresis parameters and magnetic anisotropy of silicate-hosted magnetite exsolutions. *Geophysical Journal International*, *229*(3), 1695–1717. https://doi.org/10.1093/gji/ggac007

Nye, J. F. (1985). *Physical properties of crystals: Their representation by tensors and matrices*. Oxford university press.

Owens, W., & Bamford, D. (1976). A discussion on natural strain and geological structure-magnetic, seismic, and other anisotropic properties of rock fabrics. *Philosophical Transactions of the Royal Society of London - Series A: Mathematical and Physical Sciences*, *283*(1312), 55–68.

Potter, D. K., & Stephenson, A. (1988). Single-domain particles in rocks and magnetic fabric analysis. *Geophysical Research Letters*, *15*(10), 1097–1100. https://doi.org/10.1029/gl015i010p01097

Rochette, P., Jackson, M., & Aubourg, C. (1992). Rock magnetism and the interpretation of anisotropy of magnetic susceptibility. *Reviews of Geophysics*, *30*(3), 209. https://doi.org/10.1029/92rg00733

Stacey, F. D., & Banerjee, S. K. (1974). *The physical principles of rock magnetism*. Elsevier.

Stephenson, A., & Potter, D. (1987). Gyroremanent magnetizations in dilute anisotropic dispersions of gamma ferric oxide particles from magnetic recording tape. *IEEE Transactions on Magnetics*, *23*(5), 3820–3830. https://doi.org/10.1109/tmag.1987.1065524

Stephenson, A., Sadikun, S., & Potter, D. K. (1986). A theoretical and experimental comparison of the anisotropies of magnetic susceptibility and remanence in rocks and minerals. *Geophysical Journal International*, *84*(1), 185–200. https://doi.org/10.1111/j.1365-246x.1986.tb04351.x

Stoner, E. C. (1945). XCVII. The demagnetizing factors for ellipsoids. *The London, Edinburgh, and Dublin philosophical magazine and journal of science*, *36*(263), 803–821. https://doi.org/10.1080/14786444508521510

Tarling, D. H., & Hrouda, F. (1993). *The magnetic anisotropy of rocks*. Chapman & Hall.

Uyeda, S., Fuller, M., Belshe, J., & Girdler, R. (1963). Anisotropy of magnetic susceptibility of rocks and minerals. *Journal of Geophysical Research*, *68*(1), 279–291. https://doi.org/10.1029/jz068i001p00279